Erik Engelhardt, Eric Elzenheimer, Johannes Hoffman, Tobias Schmidt, Adrian Zaman, Norbert Frey, and Gerhard Schmidt*

A Concept for Myocardial Current Density Estimation with Magnetoelectric Sensors

https://doi.org/10.1515/cdbme-2023-1023

Abstract: In this paper we present a novel noninvasive approach to estimate current densities in the heart from magnetocardiography. The proposed algorithm uses nested optimization to model current densities in equally-sized voxels of myocardial tissue. First-order Thiran all-pass filters are used to describe the propagation between voxels. We demonstrate feasibility of the algorithm for a noise-free single-layer simulation. However, challenges remain, such as addressing measurement noise and optimizing propagation velocity. Overall, this approach has the potential to complement or replace invasive catheter-based electrophysiological studies for localization of arrhythmogenic tissue.

Keywords: Biomagnetism, Magnetocardiography (MCG), Magnetoelectric (ME) Sensors, Noninvasive cardiac diagnostics

1 Introduction

Measurement of cardiac electrical activity is critical for medical purposes, especially for localization of arrhythmogenic tissue. However, invasive procedures such as cardiac catheterization are associated with risks, making a noninvasive alternative desirable. Therefore, a mapping must be found between the body surface potential measured by electrocardiogram (ECG) or the magnetic fields generated by the heart measured by magnetocardiogram (MCG) and the cardiac surface potential or myocardial current densities [1].

***Corresponding author: Gerhard Schmidt,** Digital Signal Processing and System Theory, Institute of Electrical Engineering and Information Technology, Faculty of Engineering, Kiel University, Kaiserstr. 2, 24143 Kiel, Germany, gus@tf.uni-kiel.de
Erik Engelhardt, Eric Elzenheimer, Johannes Hoffman, Tobias Schmidt, Digital Signal Processing and System Theory, Institute of Electrical Engineering and Information Technology, Faculty of Engineering, Kiel University, Kaiserstr. 2, 24143 Kiel, Germany, {eren, ee, jph, tsc}@tf.uni-kiel.de
Adrian Zaman, Medical Department III specialised in Cardiology and Angiology, University Medical Center Schleswig-Holstein, Arnold-Heller-Str. 3 / House K3, 24105 Kiel, Germany, Adrian.Zaman@uksh.de
Norbert Frey, Internal Medicine III: Heart, Vascular and Lung, University Medical Center Heidelberg, Im Neuenheimer Feld 410, 69120 Heidelberg, Germany, norbert.frey@med.uni-heidelberg.de

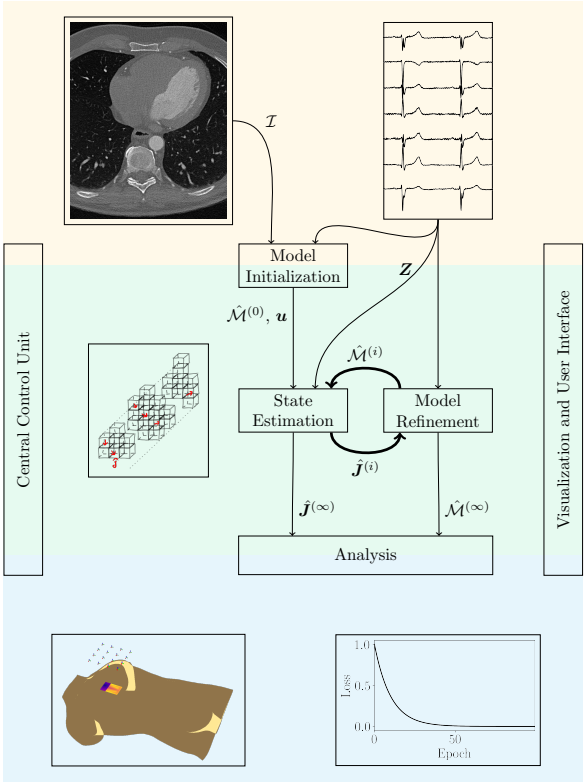

Fig. 1: Schematic overview of the current density estimation algorithm. Yellow regions represent required inputs, green regions indicate calculations, and blue regions denote outputs.

To this end, various approaches have been developed by research groups around the world, each with its own advantages and disadvantages. For example, the deep learning approach by Chen et al. [2] requires simultaneously recorded body and heart surface potentials, and the electrophysiologically realistic model by Gillette et al. [3] uses parameter sampling to fit the model to specific individuals.

While ECG is well established in routine clinical practice, MCG continues to face significant challenges due to the limited availability of suitable room temperature magnetometers. A major drawback of SQUIDs and newer optical magnetometry technology is the need for a magnetically shielded environment [4]. Magnetoelectric (ME) sensors, although not yet capable of measuring an unaveraged cardiac signal, are becoming a potential candidate for biomagnetometry [5].

In this paper, we present a novel approach based on nested optimization to estimate the current density in cardiac muscle tissue using magnetic measurements. We demonstrate the validity of this approach using a simplified simulation.

2 Methods

The general function of the proposed algorithm (cf. Fig. 1) involves computing an initial state space model $\mathcal{M}^{(0)}$ and a control function $\boldsymbol{u}$ from segmented tomographic data $\mathcal{I}$ and magnetic measurements $\boldsymbol{Z} = [\boldsymbol{z}(0),\, \boldsymbol{z}(1),\, \ldots,\, \boldsymbol{z}(N_\mathrm{m}-1)]$, where N_m is the number of consecutive measurements. Each magnetic measurement $\boldsymbol{z}(n) = [z_0(n),\, \ldots,\, z_{N_\mathrm{s}-1}(n)]^\intercal$ consists of N_s values, where N_s is the number of sensors. Furthermore, $\boldsymbol{z} = \boldsymbol{d} + \boldsymbol{s}$, where $\boldsymbol{d}$ is the desired signal, i.e., the magnetic field generated by the human heart, and $\boldsymbol{s}$ is the noise signal.

The myocardial tissue is divided into N_v equally sized voxels v, each of which is assigned one of the types shown in Fig. 2.

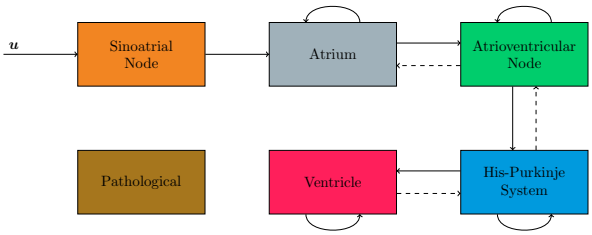

Fig. 2: Schematic description of the assumed voxel types and connectivities. The sinoatrial (SA) node is connected to the control function $\boldsymbol{u}$, which is calculated using *Myokit* [6]. The solid arrows represent connections present in healthy hearts, whereas the dashed arrows represent connections realized only in pathologies.

For each voxel, the three-dimensional current density $\boldsymbol{j}_v(n) = [j_{v,\mathrm{x}}(n), j_{v,\mathrm{y}}(n), j_{v,\mathrm{z}}(n)]^\intercal$ is tracked. The vector $\boldsymbol{j} = \left[\boldsymbol{j}_0^\intercal(n),\, \ldots,\, \boldsymbol{j}_{N_\mathrm{v}-1}^\intercal(n)\right]^\intercal$ denotes the concatenation of these individual current densities and the matrix $\boldsymbol{J} = [\boldsymbol{j}(0),\, \ldots,\, \boldsymbol{j}(N_\mathrm{m}-1)]$ all current densities over time. For readability, we omit these indices and use j to refer to the current density in a particular voxel and direction.

Assuming a sufficiently high sampling rate, in regard to the propagation velocities, the current density of each voxel affects only those in neighboring voxels. To allow for arbitrary propagation paths and velocities, the influence between voxels is modeled using first-order Thiran all-pass filters [7]. The outputs of the filters $\boldsymbol{y}$ are calculated using the equation (1). The parameters $\boldsymbol{k}$ define the integer part of the delays $\boldsymbol{\tau}$ between voxels, and the parameters $\boldsymbol{b}$ are used to define the fractional part of the delays. For each voxel, $243 = 3^5$ all-pass filters are computed. Three each for the x, y and z offsets and for the input and output directions. The vector $\boldsymbol{y}_v$ specifies all all-pass filters corresponding to one voxel v. Using these outputs, the new current densities are calculated according to equation (2). The sparse matrix $\boldsymbol{C}_v$ contains the 243 gains c that determine how strongly the voxel v is coupled to its neighbors.

$$y(n) = b \cdot \Big(j(n-k-1) - y(n-1)\Big) + j(n-k-2) \quad (1)$$

$$\boldsymbol{j}_v(n) = \boldsymbol{C}_v \boldsymbol{y}_v(n) \quad (2)$$

Delays $\boldsymbol{\tau}$ and gains $\boldsymbol{c}$ are chosen to account for physiologically normal propagation velocities ($0.1\,\mathrm{m/s} \ldots 4\,\mathrm{m/s}$) and propagation paths (cf. Fig. 2). The Biot-Savart law is used to calculate an estimated measurement matrix $\hat{\boldsymbol{H}}$. Using this matrix, the estimated desired signals $\hat{\boldsymbol{d}}(n)$, i.e., the magnetic fields generated by the human heart, can be calculated according to equation (3).

$$\hat{\boldsymbol{d}}(n) = \hat{\boldsymbol{H}} \hat{\boldsymbol{j}}(n) \quad (3)$$

The nested optimization process consists of the alternate execution of the *State Estimation* and *Model Refinement* blocks. In the *State Estimation* block, a Kalman filter is used to estimate the current densities $\hat{\boldsymbol{J}}^{(i)}$ for a given model $\hat{\mathcal{M}}^{(i)}$, a control function $\boldsymbol{u}$, and measurements $\boldsymbol{Z}$. The *Model Refinement* block then computes the loss $\mathcal{L}^{(i)}$ according to Equation (4), where $\hat{\boldsymbol{D}} = \left[\hat{\boldsymbol{d}}(0),\, \ldots,\, \hat{\boldsymbol{d}}(N_\mathrm{m}-1)\right]$. The gradient of this loss function is then used to update the parameters of the model.

$$\mathcal{L}^{(i)} = \frac{1}{N_\mathrm{m}} \frac{1}{N_\mathrm{s}} \left\| \boldsymbol{Z} - \hat{\boldsymbol{D}}^{(i)} \right\|_2^2 \quad (4)$$

When convergence or another termination criterion is met, the estimated current densities $\hat{\boldsymbol{J}}^{(\infty)}$ are submitted for further analysis along with the current model $\hat{\mathcal{M}}^{(\infty)}$.

3 Simulation

To demonstrate the feasibility of the algorithm, we simulate two single-layer models consisting of $N_\mathrm{v} = 962$ voxels with an edge length of $2.5\,\mathrm{mm}$. The magnetic field is simulated in three directions at 108 positions over the torso, yielding $N_\mathrm{s} = 324$ measurements. With a sampling frequency of $f_\mathrm{s} = 2000\,\mathrm{Hz}$ and a duration of $T = 1\,\mathrm{s}$, $N_\mathrm{m} = 2000$ time steps are calculated. The model is initialized based on the start model $\hat{\mathcal{M}}^0$ (Fig. 3a) and the measurements $\boldsymbol{Z}$ are simulated based on the target model $\mathcal{M}$ (Fig. 3b).

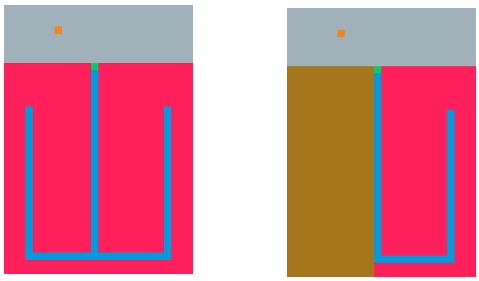

(a) $\hat{\mathcal{M}}^{(0)}$ (b) $\mathcal{M}$

Fig. 3: Used voxel types of the healthy start model (a) and the pathological target model (b). The colors of the voxels correspond to their respective types (cf. Fig. 2).

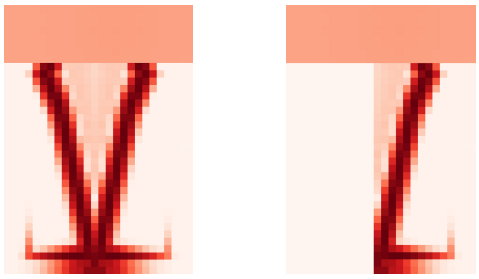

(a) $\left\|\hat{\boldsymbol{j}}_v^{(0)}(\mathrm{n_R})\right\|_2$ (b) $\left\|\boldsymbol{j}_v(\mathrm{n_R})\right\|_2$

Fig. 5: Absolute current densities for each voxel during the R-peak for the start model (a) and the target model (b). Red represents higher absolute current densities.

As control function $\boldsymbol{u}$, we use the scaled and low-pass filtered absolute derivative of the action potential of a healthy ventricular cell calculated with *Myokit* [6] using the dynamic O'Hara-Rudy model [8] (cf. Fig. 4).

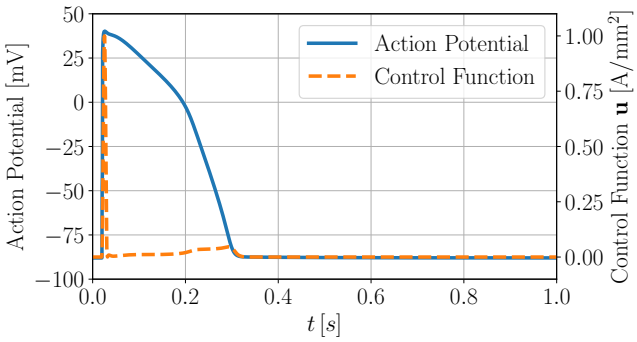

Fig. 4: Assumed action potential shape and derived control function $\boldsymbol{u}$.

We do not consider measurement noise in this study. It holds that $\boldsymbol{d} = \boldsymbol{z}$. Therefore, the updating part of the Kalman filter cannot be applied. In the *State Estimation* block, the system states are predicted based on the model only.

The only difference between the target and the initial model is in the gains of the all-pass filter $\boldsymbol{c}$. The gains are optimized according to Equation (5), while other parameters remain fixed. The two-part optimization loop is executed for 20 000 iterations with a learning rate of $\eta = 1 \cdot 10^7$.

$$\hat{c}^{(i+1)} = \hat{c}^{(i)} - \eta \frac{\partial \mathcal{L}^{(i)}}{\partial \hat{c}^{(i)}} \tag{5}$$

4 Results

The resulting absolute current densities of each voxel during the R-peak $\|\boldsymbol{j}_v(\mathrm{n_R})\|_2$ are shown in Fig. 5. Whereas the start (healthy) model $\hat{\mathcal{M}}^{(0)}$ shows symmetrical excitation, the target (pathological) model $\mathcal{M}$ lacks excitation of the right ventricle. Excitation propagation along the His-Purkinje System (HPS) is significantly faster than that through the ventricles. The current density in the atrium during the R-peak is due to its repolarization.

The simulated magnetic measurements are shown in Fig. 6 as an example for one sensor position. Although the model is very simplified, the general shape of the sinusoidal rhythm with P-, R-, and T-peaks can be seen. The main difference between the target and start model measurements can be seen during the R-peak, with smaller deviations during the T-peak.

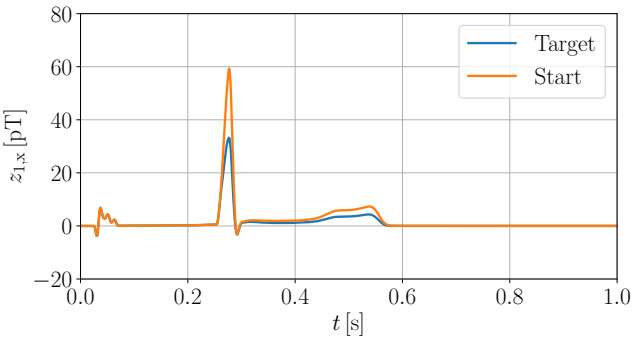

Fig. 6: Simulated magnetic fields for one sensor position in x direction for the start model and target model.

As shown in Fig. 7, the loss $\mathcal{L}$ decreases exponentially over the iterations. After 20 000 iterations, the loss is still decreasing. This suggests that the Model $\hat{\mathcal{M}}$ has not yet converged and that further iterations could improve the result.

Fig. 8 shows the maximum of the absolute current densities per voxel $\max_n \{\|\boldsymbol{j}_v(n)\|_2\}$. The start model assumes that this maximum is the same for each voxel (cf. Fig. 8a), whereas the target model has no current densities in the right ventricle (cf. Fig. 8b). Over several iterations, the gains of the all-pass filters are gradually adjusted to reduce the loss $\mathcal{L}$. This leads to

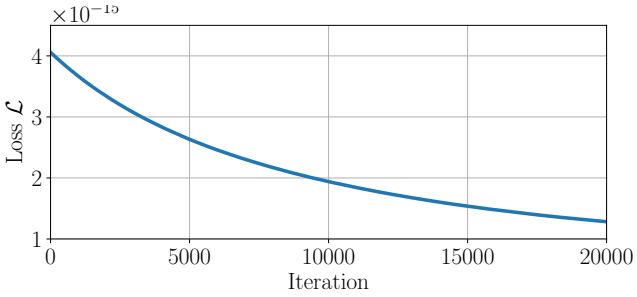

Fig. 7: The computed loss per iteration.

the maxima shown in the second row of Fig. 8. As optimization proceeds, the distribution of the estimated model becomes more similar to the distribution of the target model. In particular, the estimated maximum current density in the right ventricle is continuously reduced. After 20 000, there are still differences between the estimated and actual current densities. Considering Fig. 7, increasing the maximum number of iterations or adjusting the learning rate η could improve convergence. In this paper, we also do not constrain parameters to physiologically reasonable values. Instead of decreasing current densities in the right ventricle, the loss can be reduced by increasing current densities in other parts of the heart. Since the maximum current density per voxel is limited by the physiology of the heart muscle, introducing a constraining term could guide the algorithm to the desired local minimum.

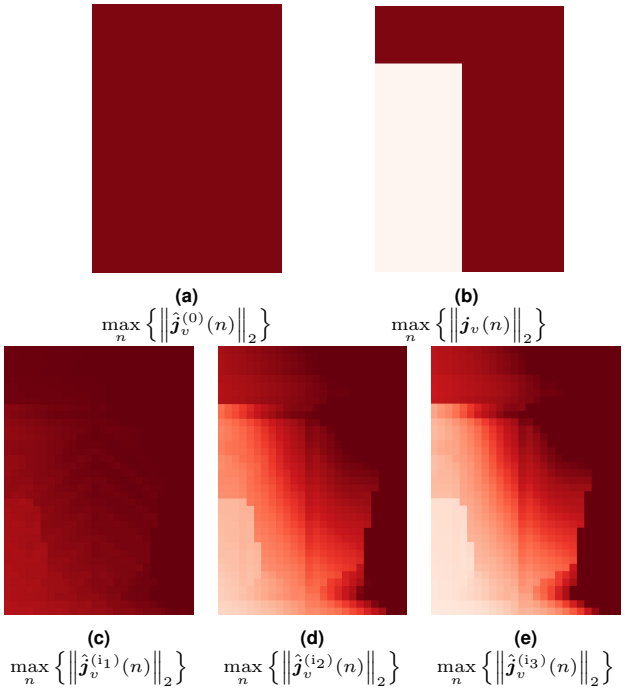

Fig. 8: The maximum absolute current densities for each voxel for the start model (a), the target model (b), and the optimized models after iterations $\mathrm{i}_1 = 691$ (c), $\mathrm{i}_2 = 10351$ (d) and $\mathrm{i}_3 = 20000$ (e).

5 Conclusion

The presented algorithm can learn the spatio-temporal evolution of current density distributions from magnetic measurements in a noise-free single-layer simulation, demonstrating the general feasibility of the approach. However, several challenges still need to be addressed. These include dependence on measurement noise, grid offset, voxel size, number of sensors, simultaneous optimization of propagation velocity and paths, and assumptions about the control function and initial propagation velocities. Overcoming these challenges could allow the proposed algorithm to complement or replace invasive electrophysiological studies for the localization of arrhythmogenic tissue. In conjunction with stereotactic body radiation therapy (SBRT), this could lead to completely noninvasive treatment of, for example, ventricular arrhythmias.

Author Statement

Research Funding: This work was funded by the German Research Foundation (Deutsche Forschungsgemeinschaft, DFG) through the Collaborative Research Center CRC 1261 Magnetoelectric Sensors: From Composite Materials to Biomagnetic Diagnostics (Project B10). Conflict of interest: Authors state no conflict of interest. Informed consent: Informed consent has been obtained from all individuals included in this study. Ethical Approval: The research involving human subjects complies with all relevant national regulations and institutional guidelines and was conducted in accordance with the principles of the Declaration of Helsinki. It was approved by the Ethics Committee of the Medical Faculty of Kiel University under Eudamed number CIV-20-04-032332.

References

[1] H. Koch and W. Haberkorn, "Magnetic field mapping of cardiac electrophysiological function," *Philosophical Transactions of the Royal Society of London. Mathematical, Physical and Engineering Sciences*, vol. 359, no. 1783, pp. 1287–1298, 2001.

[2] K.-W. Chen, L. Bear, and C.-W. Lin, "Solving Inverse Electrocardiographic Mapping Using Machine Learning and Deep Learning Frameworks," *Sensors*, vol. 22, no. 6, p. 2331, Mar. 2022. [Online]. Available: https://www.mdpi.com/1424-8220/22/6/2331

[3] K. Gillette, M. A. Gsell, A. J. Prassl, E. Karabelas, U. Reiter, G. Reiter, T. Grandits, C. Payer, D. Štern, M. Urschler, J. D. Bayer, C. M. Augustin, A. Neic, T. Pock, E. J. Vigmond, and G. Plank, "A Framework for the generation of digital twins of cardiac electrophysiology from clinical 12-leads ECGs," *Medical Image Analysis*, vol. 71, p. 102080, Jul. 2021. [Online]. Available: https://linkinghub.elsevier.com/retrieve/pii/S1361841521001262

[4] E. Elzenheimer, C. Bald, E. Engelhardt, J. Hoffmann, P. Hayes, J. Arbustini, A. Bahr, E. Quandt, M. Höft, and G. Schmidt, "Quantitative Evaluation for Magnetoelectric Sensor Systems in Biomagnetic Diagnostics," *Sensors*, vol. 22, no. 3, p. 1018, Jan. 2022. [Online]. Available: https://www.mdpi.com/1424-8220/22/3/1018

[5] E. Elzenheimer, P. Hayes, L. Thormahlen, E. Engelhardt, A. Zaman, E. Quandt, N. Frey, M. Hoft, and G. Schmidt, "Investigation of Converse Magnetoelectric Thin-Film Sensors for Magnetocardiography," *IEEE Sensors Journal*, vol. 23, no. 6, pp. 5660–5669, Mar. 2023. [Online]. Available: https://ieeexplore.ieee.org/document/10028750/

[6] M. Clerx, P. Collins, E. de Lange, and P. G. Volders, "Myokit: A simple interface to cardiac cellular electrophysiology," *Progress in Biophysics and Molecular Biology*, vol. 120, no. 1-3, pp. 100–114, Jan. 2016. [Online]. Available: https://linkinghub.elsevier.com/retrieve/pii/S0079610715002576

[7] J.-P. Thiran, "Recursive digital filters with maximally flat group delay," *IEEE Transactions on Circuit Theory*, vol. 18, no. 6, pp. 659–664, 1971. [Online]. Available: http://ieeexplore.ieee.org/document/1083363/

[8] T. O'Hara, L. Virág, A. Varró, and Y. Rudy, "Simulation of the Undiseased Human Cardiac Ventricular Action Potential: Model Formulation and Experimental Validation," *PLoS Computational Biology*, vol. 7, no. 5, p. e1002061, May 2011. [Online]. Available: https://dx.plos.org/10.1371/journal.pcbi.1002061